Dense and pure high-entropy metal diboride ceramics sintered from self-synthesized powders *via* boro/carbothermal reduction approach

Junfeng Gu[1], Ji Zou[1,2*], Shi-Kuan Sun[3], Hao Wang[1], Su-Yang Yu[2], Jinyong Zhang[1], Weimin Wang[1] and Zhengyi Fu[1*]

ABSTRACT Equimolar quinary diboride powders, with nominal composition of $(Ti_{0.2}Hf_{0.2}Zr_{0.2}Nb_{0.2}Ta_{0.2})B_2$, were synthesized by boro/carbothermal reduction (BCTR) of oxide mixtures (MO_x, M = Ti, Hf, Zr, Nb and Ta) using B_4C as source of B and C in vacuum. By adjusting the B_4C/MO_x ratios, diboride mixtures without detectable MO_x were obtained at 1600°C, while high-entropy diboride (HEB) powders with particle size of < 1 μm was obtained at 1800°C. The phase, morphology and solid solution evolution process of the HEB powders during the BCTR process were comprehensively investigated. Although X-ray diffraction pattern indicated the powders synthesized at 1800°C were in a single-phase AlB_2 structure, elemental mappings showed that (Ta, Ti)-rich and (Zr, Nb)-rich solid solution coexisted in the HEB powders. The distribution of niobium and zirconium atoms in HEB was unable to reach uniform until the HEB powders were spark plasma sintered at 2000°C. $(Ti_{0.2}Hf_{0.2}Zr_{0.2}Nb_{0.2}Ta_{0.2})B_2$ ceramics with a relative density of 97.9% were obtained after spark plasma sintering the HEB powders at 2050°C under 50 MPa. Rapid grain growth was found in this composition when the sintering temperature was increased from 2000 to 2050°C, and the averaged grain size increased from 6.67 to 41.2 μm. HEB ceramics sintered at 2000°C had a Vickers hardness of 22.44 ± 0.56 GPa (under a load of 1 kg), a Young's modulus of ~500 GPa and a fracture toughness of 2.83 ± 0.15 MPa m$^{1/2}$. This is the first report for obtaining high density HEB ceramics without residual oxide phase, benefiting from the high quality HEB powders obtained.

Keywords: ultra-high temperature ceramics, high-entropy borides, solid solution, rapid grain growth, powder synthesis

INTRODUCTION

High-entropy alloys (HEAs) have attracted much research interest in recent years. Although the effects of "entropy stabilized" are still controversial, some HEAs exhibit superior mechanical and physical properties [1–3]. HEAs refer to the solid solutions that are formed by mixing equal or relatively large proportions of five or more metallic elements [1–4]. The concept of high-entropy ceramics (HECs) was extended from HEAs. Up to now, studies on the preparation and characterization of HECs including oxides [5–14], carbides [15–21], borides [22–26], nitrides [27–29], and silicides [30] have been extensively carried out. Analogous to HEAs, HECs also show some unique properties including high hardness [15,16,20,22] and excellent thermo-mechanical properties [16], implying their promising applications in various areas including cutting tool [16], thermal protecting coating [24,28], etc.

High-entropy metal diborides (HEBs) were the firstly proposed and synthesized high-entropy non-oxides, which have greatly broadened the scope of high-entropy materials and the family of ultra-high temperature ceramics (UHTCs) [22]. These transition metal diborides exhibit a unique layered hexagonal crystal structure with alternating rigid two-dimensional (2D) boron nets and high-entropy 2D layers of metal cations [22]. Up to now, a series of HEBs including $(Ti_{0.2}Hf_{0.2}Zr_{0.2}Nb_{0.2}Ta_{0.2})B_2$, $(Hf_{0.2}Zr_{0.2}Ta_{0.2}Mo_{0.2}Ti_{0.2})B_2$, $(Hf_{0.2}Zr_{0.2}Mo_{0.2}Nb_{0.2}Ti_{0.2})B_2$, $(Hf_{0.2}Mo_{0.2}Ta_{0.2}Nb_{0.2}Ti_{0.2})B_2$, $(Mo_{0.2}Zr_{0.2}Ta_{0.2}Nb_{0.2}Ti_{0.2})B_2$, $(Hf_{0.2}Zr_{0.2}Ta_{0.2}Cr_{0.2}Ti_{0.2})B_2$, and $(Zr_{0.23}Ti_{0.20}Hf_{0.19}V_{0.14}Ta_{0.24})B_2$ have been obtained [22–26]. These diborides show higher hardness and better oxidation resistance than the average

[1] State Key Laboratory of Advanced Technology for Materials Synthesis and Processing, Wuhan University of Technology, Wuhan 430070, China
[2] School of Metallurgy and Materials, University of Birmingham, Birmingham B15 2TT, United Kingdom
[3] Department of Materials Science and Engineering, University of Sheffield, Sheffield S1 3JD, United Kingdom
* Corresponding authors (emails: j.zou@bham.ac.uk or zouji1983@aliyun.com (Zou J); zyfu@whut.edu.cn (Fu Z))

performance of five individual counterparts [22]. HEB also offers a large space to tune the properties of diborides through controlling the composition of the solid solutions. In addition, reports confirmed that some unstable diborides like MoB_2, could be stabilized at an AlB_2 structure in HEB [22,25]. This kind of cations, if segregated at grain boundary, might improve the mechanical property and oxidation resistance of UHTCs [31].

However, similar to other transitional metal diborides, the fabrication of dense HEB bulks still faces a challenge due to the impurities in starting powders and the strong covalent bonding therein. For example, all the aforementioned HEB ceramics densified from single phase diborides reached about ~92% of final relative density, although the starting powders had been ground to a fine level through high energy ball-milling [22]. Tallarita et al. [25] proposed a new processing route to densify HEBs that combined self-propagating high-temperature synthesis (SHS) with spark plasma sintering (SPS). Although the processing time had been shortened since ball-milling process was no more needed, the final relative density of HEBs did not exceed 92.5%.
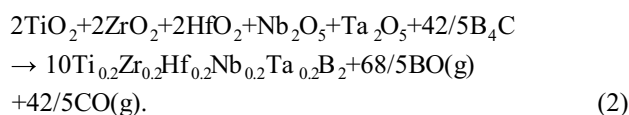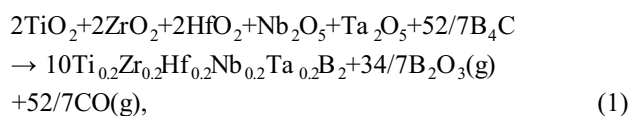
The presence of porosity and impurities might make us greatly underestimate/misunderstand some performances of HEBs. High quality starting powder is the prerequisite to obtain HEBs with high purity and density. Boro/carbothermal reductions (BCTR) have been widely used for the synthesis of transition metal diboride powders [32–36]. However, this approach has not been well explored to synthesize HEB powders. Recently, Zhang et al. [26] showed that HEBs with relative density above 95% including $(Hf_{0.2}Zr_{0.2}Ta_{0.2}Cr_{0.2}Ti_{0.2})B_2$, $(Hf_{0.2}Zr_{0.2}Mo_{0.2}Nb_{0.2}Ti_{0.2})B_2$ and $(Mo_{0.2}Zr_{0.2}Ta_{0.2}Nb_{0.2}Ti_{0.2})B_2$ could be sintered from HEB powders that were synthesized via borothermal reduction. Nevertheless, all the HEB ceramics from reference [26] show the presence of oxide impurities up to 7.2 wt%.

Therefore, the present work has two purposes: (1) to develop a feasible BCTR route for fine HEB powders to minimize the oxide levels and (2) to investigate the solid solution formation and densification behavior of the as-

synthesized powders to achieve dense HEBs with a finer microstructure.

EXPERIMENTAL SECTION

Commercially available TiO_2 (99.9% purity, $D_{50} = 50$ nm, Aladdin, China), ZrO_2 (99.9% purity, $D_{50} = 50$ nm, CSG Holding, China), HfO_2 (99.9% purity, average gain size 300 nm, Founde Star, China), Nb_2O_5 (99.9% purity, Aladdin, China), Ta_2O_5 (99.9% purity, Aladdin, China), and B_4C (97% purity, average gain size 2.36 μm, Mudanjiang Diamond Boron Carbide, China) powders were used as raw materials. It should be noted that the reactions between B_4C and oxides at higher temperature in vacuum can generate both B_2O_3 and BO. If only B_2O_3 is formed during the BCTR process, the process should proceed according to Reaction (1); vice versa, if BO is the only gaseous product, Reaction (2) should take place.

$$2TiO_2+2ZrO_2+2HfO_2+Nb_2O_5+Ta_2O_5+52/7B_4C$$
$$\rightarrow 10Ti_{0.2}Zr_{0.2}Hf_{0.2}Nb_{0.2}Ta_{0.2}B_2+34/7B_2O_3(g)$$
$$+52/7CO(g), \qquad (1)$$

$$2TiO_2+2ZrO_2+2HfO_2+Nb_2O_5+Ta_2O_5+42/5B_4C$$
$$\rightarrow 10Ti_{0.2}Zr_{0.2}Hf_{0.2}Nb_{0.2}Ta_{0.2}B_2+68/5BO(g)$$
$$+42/5CO(g). \qquad (2)$$

In order to minimize both the residual B_4C and MO_x in the final powders, the B_4C/MO_x ratio should be set in the range regulated by Reactions (1) and (2). Accordingly, four compositions with different B_4C/MO_x ratios denoted as HEB1, HEB2, HEB3 and HEB4 were designed. Corresponding molar ratios of $TiO_2/ZrO_2/HfO_2/Nb_2O_5/Ta_2O_5/B_4C$ are 2/2/2/1/1/7.43 (all B_2O_3, Reaction (1)), 2/2/2/1/1/7.8, 2/2/2/1/1/8.17, and 2/2/2/1/1/8.4 (all BO, Reaction (2)). The designations for the different specimens are listed in Table 1.

The mixtures (each for 100 g) were blended in a ball-miller for 12 h, using ethanol and ZrO_2 balls with a diameter of 5 mm as the mixing media. The weight loss of ZrO_2 balls after mixing for 12 h was less than 0.1 g. After mixing, rotary evaporation was used to remove the excess solvent from the mixture. Then, the mixtures were

Table 1 Sample designations

Composition	$TiO_2/ZrO_2/HfO_2/Nb_2O_5/Ta_2O_5/B_4C$	Excess B_4C	1300°C	1400°C	1500°C	1600°C	1700°C	1800°C
HEB1[a]	2/2/2/1/1/7.43	0 wt%	HEB1-13	HEB1-14	HEB1-15	HEB1-16	HEB1-17	HEB1-18
HEB2	2/2/2/1/1/7.8	5 wt%	HEB2-13	HEB2-14	HEB2-15	HEB2-16	HEB2-17	HEB2-18
HEB3	2/2/2/1/1/8.17	10 wt%	HEB3-13	HEB3-14	HEB3-15	HEB3-16	HEB3-17	HEB3-18
HEB4[b]	2/2/2/1/1/8.4	13 wt%	HEB4-13	HEB4-14	HEB4-15	HEB4-16	HEB4-17	HEB4-18

a) According to Reaction (1); b) according to Reaction (2).

ground in an agate mortar by pestle and sieved through a 200-mesh screen. Field-assisted synthesis has been proven to be efficient for the fast synthesis of high purity UHTC powders [37,38]. In this work, a quantity of 20 g mixtures for each composition was then placed in a graphite crucible for reduction processing in a SPS system (ED-PAS-111, ELENX, Japan). The details for the setup could be found in our previous work [39,40]. This experiment was conducted in vacuum with a heating rate of 100°C/min to the designed temperature and held for 10 min. The initial vacuum reading was ~10 Pa. This number dropped when the reduction process started during heating, and the maximum vacuum level reached ~300 Pa during the powder synthesis. After holding at 1700°C or above, the vacuum level returned to ~10 Pa. The temperature was monitored by an optical pyrometer focusing on the external wall of the graphite crucible. Finally, 2.5 g of powders for each pellet was poured into a graphite die with inner diameter of 15 mm and densified using the same furnace: the sintering temperatures were 1900, 2000 and 2050°C, with a heating rate of 100°C/min and holding time of 5 min.

The phase assembly of the as-prepared samples was examined by X-ray diffraction (XRD, Empyrean, Pana-lytical, Netherlands). The microstructure was investigated by a scanning electron microscope (SEM, JEOL7000F, Tokyo, Japan) equipped with energy/wavelength-dispersive X-ray (EDS/WDS, Oxford, UK) analyzer system and a scanning transmission electron microscope (STEM, TalosF200S, FEI, USA). Final density of the bulks was measured using the Archimedes' method. Oxygen and carbon contents in the selected powder samples were measured by a nitrogen/oxygen determinator (TC600, Leco Corporation, USA) and a carbon/sulphur analyzer (CS-2000, Eltra Elemental Analyzers, Germany), respectively. Theoretical densities of HEBs were calculated according to the lattice parameters of HEB3, by fitting the peaks from the XRD results. XRD patterns were analyzed using Rietveld refinement method [41]. The program EXPGUI 2 was used to refine a structural model based on ZrB_2 (in hexagonal space group $P6/mmm$) [42]. On basis of the calculated lattice parameter, the theoretical density was determined by the quotient between unit cell mass and unit cell volume. The thermodynamic calculations were performed *via* HSC Chemistry v. 7.1 (Outokumpu research Oy, Pori, Finland).

The grain size was measured from the SEM images. Each reported value was averaged from ~400 grains. The modulus and Vickers hardness of the as-sintered ceramics were determined by a mechanical resonance frequencies machine (GrindoSonic, Model MK7, Sweden) and a Vickers Hardness Tester (Durascan50, Struers, Austria), respectively. For the hardness test, hardness values were compared under different loads (0.2, 1 and 5 kg) at the same holding time of 15 s. The fracture toughness of HEB was calculated by direct crack measurements according to Anstis equation [43], based on the crack generated by the indents with a load of 5 kg. A typical indentation image for the crack measurement was shown in Fig. S1.

RESULTS AND DISCUSSION

Thermodynamic consideration

Though all the MO_x could be reduced by B_4C with increasing temperature, the favorable temperatures for the different BCTR reactions are different. Equilibrium amounts of phases in MO_x-B_4C system were calculated as a function of temperature (Fig. 1a) under a system partial pressure of 10 Pa. The prediction shows that the reaction between Ta_2O_5 and B_4C at P = 10 Pa could start even at room temperature, so does the reaction between Nb_2O_5 and B_4C. The required temperature for the reduction of MO_x by B_4C increases in an order of TiO_2, ZrO_2 and HfO_2. The proceeding of the HfO_2-B_4C reduction is the most difficult; a temperature over 1000°C is needed.

If the input amount of the raw materials is based on Reaction (1), the calculation also implies that certain amounts of ZrO_2 and HfO_2 gradually reappear in the system when temperature exceeds 1100°C. Interestingly, the increasing amounts of ZrO_2 and HfO_2 are associated with the occurrence of BO(g). At a sufficiently high temperature, B_2O_3(l, g) could react with B_4C to generate BO(g). When it happens, more B_4C will be consumed. The lack of B_4C is the reason for the occurrence of ZrO_2 and HfO_2 in Fig. 1a when temperature is over 1100°C. It is the theoretical basis for adding excess B_4C in the starting powder mixtures, in order to obtain HEB powders free of residual oxides, as will be described later.

The reaction order in MO_x-B_4C system at 1600°C can be seen from Fig. 1b. As shown in the plots, among MO_x, Nb_2O_5 is the easiest compound which could be reduced by B_4C, followed by Ta_2O_5, TiO_2, ZrO_2 and HfO_2. It should be noted that no solid solutions of various oxides or diborides were considered in these calculations (Fig. 1), due to the lack of thermodynamic database. Solid solutions normally have lower Gibbs' free energies compared with the end members; therefore, more complicated oxide or boride solid solutions may co-exist in MO_x-B_4C system, which fail to be taken into account from the current calculations.
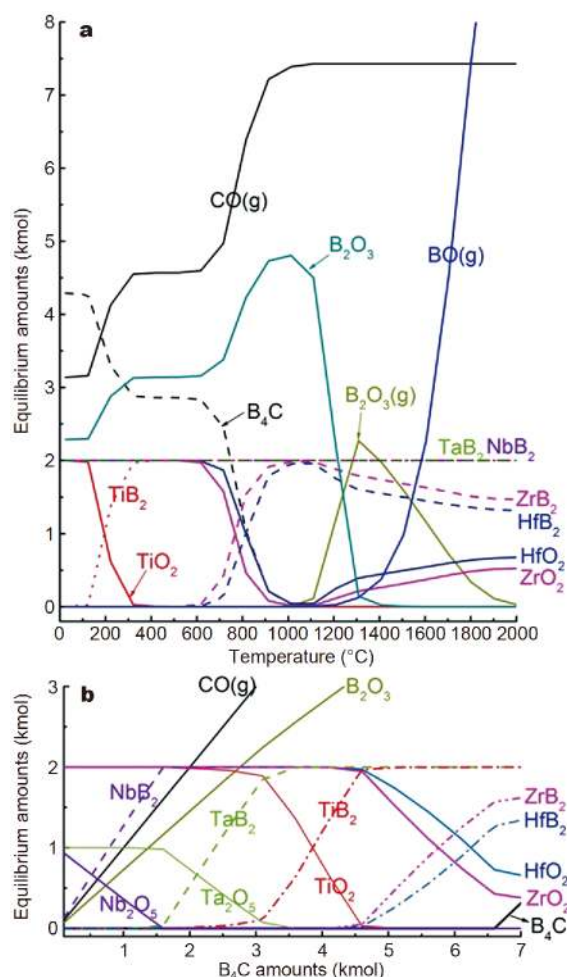
Figure 1 (a) Molar content of the products in equilibrium as a function of the temperature from room temperature (RT) to 2000°C at a partial pressure of 10 Pa. The input amounts of the reactants are based on Reaction (1). (b) The effects of B_4C amount on the progress of reactions in MO_x-B_4C system at 1600°C.

Reaction process

Fig. 2a shows the XRD patterns for the powders synthesized at 1800°C. Peaks for residual oxides were found in HEB1-18 and HEB2-18, but disappeared when more B_4C were added in the starting mixtures (HEB3-18 and HEB4-18), indicating the reactions proceeded according to both Reactions (1) and (2). The optimized excess amount of B_4C to completely remove MO_x based on Reaction (1) should be in a range from 5 to 10 wt%. No apparent peak shift was detected among HEB1–HEB4, as seen from an enlarged range in Fig. 2b, indicating the compositions of the high-entropy diboride phase (AlB_2 structure with a space group of $P6/mmm$, solid solution 1, SS1) were similar when different B_4C/MO_x ratios were adopted. However, the peak assigned to the (101) plane in Fig. 2b

reveals the presence of trace unsolved boride (SS2) in HEB1-18 and HEB2-18. Based on the XRD patterns of HEB3-18, lattice parameters of $(Ti_{0.2}Zr_{0.2}Hf_{0.2}Nb_{0.2}Ta_{0.2})B_2$ were refined as $a=3.1062 \pm 0.0013$ Å and $c=3.3755 \pm 0.0021$ Å, slightly higher than those in Gild's work ($a=3.101$ Å, $c=3.361$ Å), but lower than the first-principle predicted values ($a=3.116$ Å, $c=3.391$ Å) [22,23]. According to the lattice parameters of HEB3-18, theoretical density of $(Hf_{0.2}Zr_{0.2}Ta_{0.2}Nb_{0.2}Ti_{0.2})B_2$ was calculated to be 8.237 g cm^{-3}, assuming the lattice is fully occupied.

The phase evolution of HEB3 at different temperatures is displayed in Fig. 2c, d. Clearly, with the increase of temperature, oxides were gradually converted into diborides, and disappeared completely at 1500°C. Interestingly, peaks assigned to TiO_2, Nb_2O_5 and Ta_2O_5 were not detectable in the mixtures at 1300°C, suggesting that the boro/carbothermal reductions of TiO_2, Nb_2O_5 and Ta_2O_5 took place earlier compared with those of ZrO_2 and HfO_2. Such observation well fits the thermodynamic prediction shown in Fig. 1. In fact, Ta_2O_5 can react with B_4C and completely convert into TaB_2 at 1100°C, while corresponding temperature for the conversion of ZrO_2 needs at least 1400°C [34,36]. The difference of favorable temperatures between thermodynamic prediction and experimental observation suggests the kinetics play a major role in the advancement of BCTR in MO_x-B_4C systems.

The contents of residual oxygen and carbon in the as-synthesized HEB3 powders are 7.52 and 0.18 wt% in HEB3-16, respectively, as listed in Table 2. The low carbon content suggested most of the B_4C in the powder mixture had been reacted with MO_x at 1600°C. Considering no oxide peaks were found in HEB3-16 (Fig. 2b), the high level of oxygen content in this sample indicated that significant amount of B_2O_3 was still left in the powders after the vacuum reduction at 1600°C. A sharp drop of the oxygen content from 7.52 to 0.64 wt% was found with the increase of synthesis temperature to 1700°C, implying most of the B_2O_3 had been removed out of the boride powders at this stage. It should be noted that the HEB3-17 powders synthesized in this work shows substantially lower oxygen/carbon content, compared with the other HEB powders prepared via various routes [35,36].

Morphology evolution of HEB powders during BCTR

The morphology of HEB3-13 powders is shown in Fig. 3a. Clearly, there are still unreacted B_4C and oxide particles as arrowed in HEB3-13. As the temperature increased, the boride particles gradually transformed into regular shapes
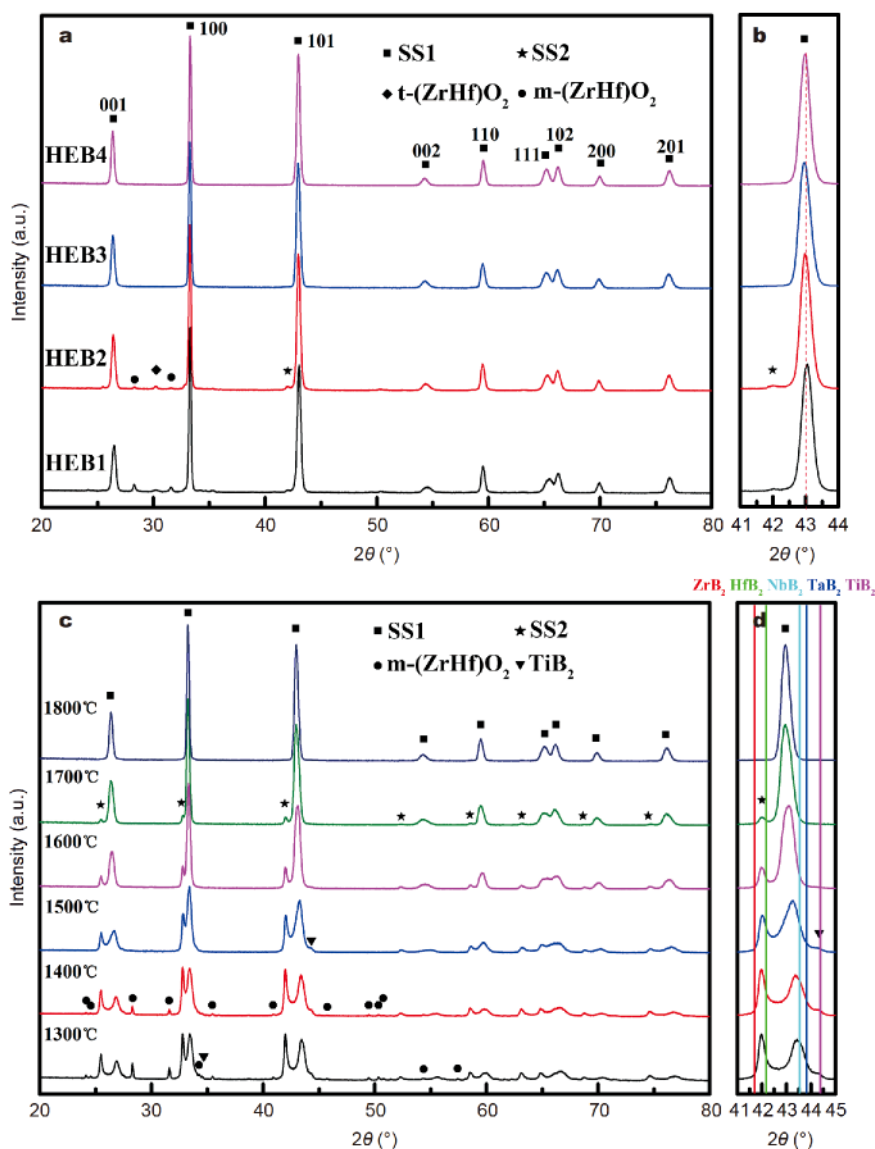
Figure 2 XRD patterns of (a, b) HEB powders synthesized at 1800°C and (c, d) HEB3 powders synthesized at 1300–1800°C.

Table 2 Oxygen and carbon contents in the selected HEB powders

Composition	Oxygen content (wt%)	Carbon content (wt%)
HEB3-16	7.52	0.18
HEB3-17	0.64	0.041
HEB3-18	0.52	0.032

and their sizes became coarser (Fig. S2a–d). When the synthesis temperature reached 1600°C (Fig. 3b), the contrast of backscattered electron signal from the powders became uniform, revealing most of the oxides and B_4C had been consumed. Interestingly, the newly formed

ultra-fine boride powders in Fig. 3a were agglomerated in a shape that resembled unreacted B_4C particles. A higher magnification image of HEB3-13 in Fig. 3c indicated the boride particles were embedded in the unreacted B_4C matrix with a darker contrast. Such phenomenon implied that the surfaces of B_4C particles were the sites where the reduction reactions took place, and boride powders were generated through the reactions between the B_4C particles and oxide particles attached on them. Inversely, if the diffusion of boron atoms into oxides is the controlling step of BCTR, grains should be observed in the shape resembling original oxides rather than B_4C. Similar features in Fig. 3c can be seen in the powders synthesized at

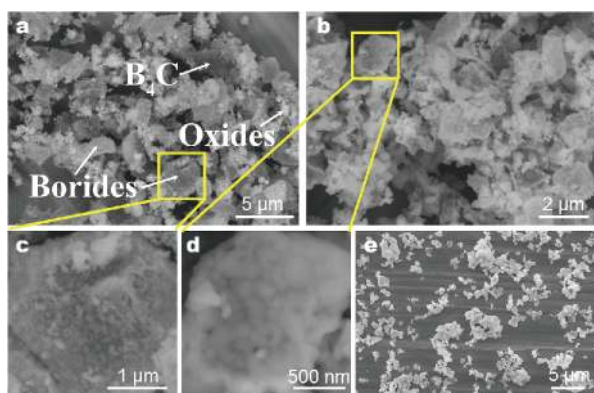**Figure 3** Back scattered electron (BSE) image of the (a) HEB3-13 and (b) HEB3-16 powders, showing the presence of unreacted oxides, unreacted B_4C and newly formed ultra-fine diboride particles as-arrowed. (c, d) Higher magnification images of the ultra-fine diboride particles in (a) and (b). (e) SEM image of the HEB3-18 powders.

1600°C (Fig. 3d), i.e., some diborides agglomerated into a shape of raw B_4C particles. However, no region with darker contrast could be recognized in HEB3-16, indicating that residual B_4C was completely consumed at 1600°C.

The morphology of the HEB powders synthesized with various amounts of B_4C additions at 1800°C is presented in Fig. 3e and Fig. S2e–g. Slight difference in morphology can be seen from these images, i.e., necking is prone to take place in the powders synthesized at higher temperature and/or with more B_4C additions. The average particle size of HEB1-18, HEB2-18, HEB3-18, and HEB4-18 powders is 0.35 ± 0.07, 0.38 ± 0.10, 0.44 ± 0.12, and 0.63 ± 0.15 μm, respectively. Fig. 4 presents the high resolution TEM (HRTEM) images of the HEB3-13 and HEB3-18 powders, both of which are well crystalline. The interplanar distances of HEB3-13 match well with those of $(\bar{1}\bar{1}0)$ and $(0\bar{1}1)$ planes of SS1 (0.208 and 0.154 nm, from XRD patterns). The interplanar distances of HEB3-18 match well with those of (100) and $(1\bar{1}1)$planes (0.269 and 0.210 nm, from XRD patterns) in HEB with AlB_2 structure.

The formation of solid solution during BCTR

Although five different oxides were used, only three different diboride phases (SS1, SS2, TiB_2, as seen in Fig. 2c) were detected from the XRD pattern of the powders synthesized at 1300°C. The relative peak intensity of SS2 and TiB_2 gradually decreased with temperature, suggesting that SS1, SS2 and TiB_2 diffused into each other to form a single-phase solid solution and such an entropy increase process was activated by temperature. According
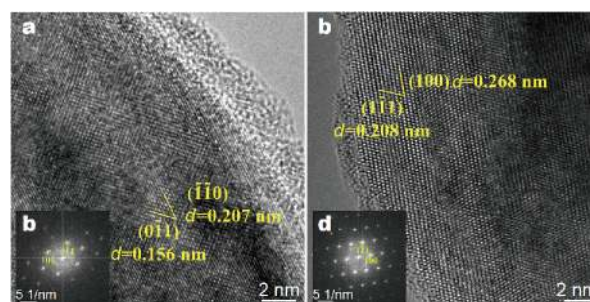

Figure 4 HRTEM images of HEB3 powders synthesized at (a) 1300 and (c) 1800°C. The fast Fourier transform images of (a) and (c) were inserted as (b) and (d).

to the XRD pattern of HEB3-13 (Fig. 2c), the lattice parameters of SS2 are a=3.1504 Å, c=3.4958 Å, slightly smaller than those of the as-reported $Zr_{0.5}Hf_{0.5}B_2$ (a=3.1542 Å, c=3.4954 Å [44] and a=3.155 Å, c=3.497 Å [45]). An enlarged region of the peaks assigned to (101) plane in Fig. 2d reveals that the peak shift of SS2 is very limited for increasing processing temperature. On the contrary, SS1 shifted significantly towards lower angles, indicating that the composition of SS2 kept almost unchanged during its diffusion into SS1. It is worth noting that intensity of $(Zr,Hf)O_2$ peaks also decreases in this temperature range. If there are other major metallic elements apart from Hf and Zr in SS2, the incorporation of more HfB_2 and ZrB_2 should cause a further peak shift of SS2 between 1300 and 1500°C. Accordingly, SS2 must be rich in HfB_2 and ZrB_2, in accordance with the evolution of the XRD patterns.

To further understand the solid solution process, STEM-mappings of HEB3-13 and HEB3-18 were chosen to evaluate the compositional uniformity in the powders after BCTR. However, the scale of HAADF-STEM mapping is not large enough to fully recognize the phase separation verified by XRD. The mappings on the different areas from HEB3-13 and HEB3-18 show the signals of five transition metal elements (Fig. 5). This indicates the formation of quinary solid solution (SS1) started at as low as 1300°C; however, the distribution of these elements in the solid solution seems to be inhomogeneous. For instance, several regions rich in Ti were found in HEB3-13 (Fig. 5a), implying the as-indexed TiB_2 in Fig. 2c actually was a solid solution but concentrated on Ti. As the temperature increased to 1800°C, the distribution of Nb was slightly different from other elements which had diffused uniformly (Fig. 5b). However, based on the XRD pattern (Fig. 2a), a single phase HEB has been indexed at this temperature.

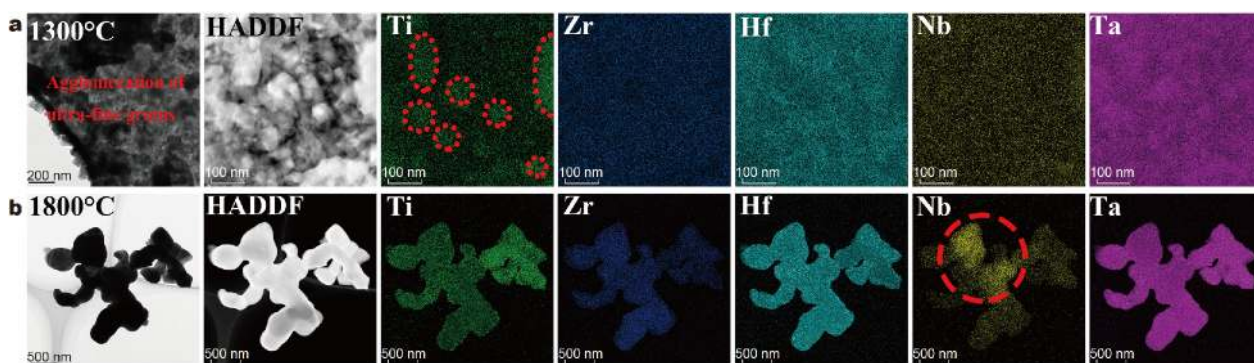The above assumption on the formation of solid solu-

Figure 5 (a) TEM image of the HEB3-13 powders shows an agglomeration of newly formed ultra-fine diborides grains. STEM-mappings of one of the agglomerate regions indicate the quinary solid solution reaction had occurred at 1300°C. (b) TEM image and STEM-mappings of the HEB3-18 powders reveal the unevenly atomic distribution within grains. Note that some circled regions have different concentrations of Nb.

tion was further examined by SEM and element mappings. In Fig. 6a, regions with different features/contrasts are identified on HEB3-13. Among them, some spherical particles (marked 3 in Fig. 6a, ~0.5 μm) are randomly distributed in the pellet, which are mainly composed of Zr, Hf and O, as indicated by the EDS patterns (Fig. 6d). Hence, these particles are likely assumed to be $(Zr,Hf)O_2$, as previously indexed from the XRD patterns. The distribution of elements in the other regions of HEB3-13 is also inhomogeneous, and two typical regions are labelled as "1" and "2" in Fig. 6b and c, respectively. EDS spectra confirm the presence of all five elements in these areas; however, region "1" is richer in Ti and Ta while Hf, Zr and Nb are the dominated metallic elements in region

"2". Combined with the XRD pattern (Fig. 2c), region "1" and "2" are likely assumed to SS1 and SS2, due to the differences in lattice parameters, i.e., the lattice parameters of ZrB_2 and HfB_2 are larger than those of TiB_2, NbB_2 and TaB_2.

If it were correct, the extents of areas rich in Hf, Zr and Nb would be obviously smaller, compared with that in TiTa-rich region in HEB3-16, due to the lower intensity of SS2 in HEB3-16 (Fig. 2c). However, it was not the case. In HEB3-16 (Fig. 7a), two regions still could be easily recognized, and the area rich in Zr and Nb is of the similar extent as that rich in Ta and Nb, although the distribution of Hf seems to be homogenous. The deconvolution of the XRD peaks for HEB3-16 also indicates
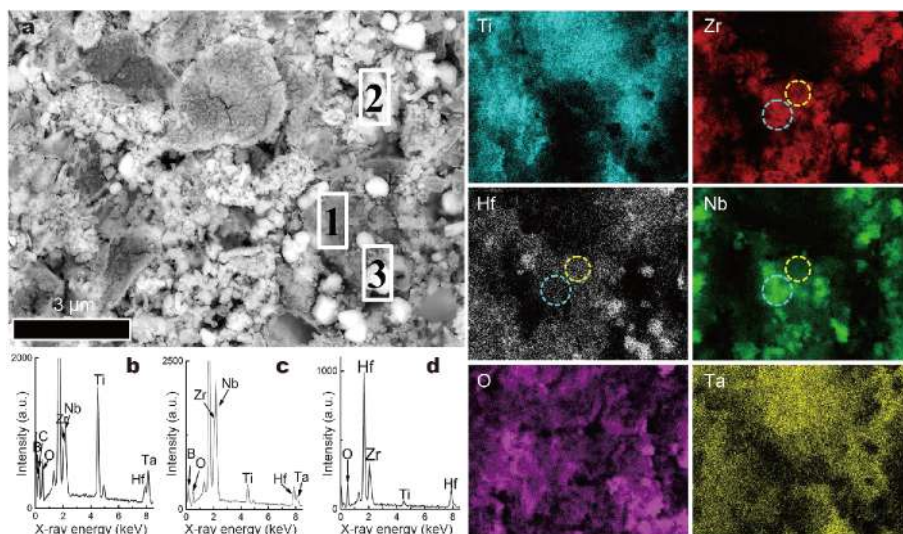

Figure 6 (a) BSE image of the HEB3-13 powders and corresponding EDS-mappings, (b–d) point EDS results showing the presence of (Ti, Ta)-rich regions, (Zr,Hf)-rich regions and unreacted $(Zr,Hf)O_2$. The circled regions in the Nb, Zr and Hf mappings revealing the ZrNb-rich smaller particles are superimposed on the ZrHfNb-rich area.
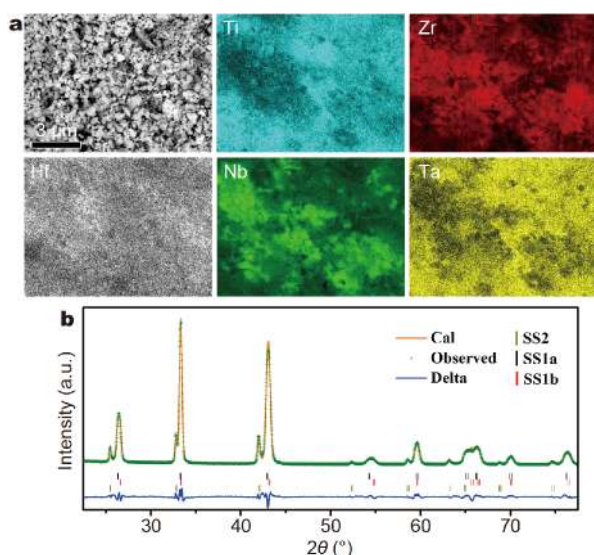
Figure 7 (a) BSE image and corresponding EDS-mappings of HEB3-16, and (b) Rietveld refinement of the XRD patterns of HEB3-16 using MAUD software (Rwp = 9.29%).

that SS1 is constituted of two parts (Fig. 7b). By further zooming the region "2" in HEB3-13, it could be found that smaller particles with stronger signals of Zr and Nb were superimposed on the ZrHfNb-rich area, as circled in the Zr, Hf and Nb mappings in Fig. 6. Therefore, apart from TiB$_2$-rich area, there are three other boride solution phases in HEB3-13 powders: (1) (Ti, Ta)-rich regions, (2) (Zr, Hf, Nb)-rich regions and (3) (Zr, Nb)-rich regions. Note that the locations of (2) and (3) are normally overlapping at 1300°C and (2) is decreasing in size with temperature increase.

According to the Vegard's law, the lattice parameters of solid solution should locate in the area among their single component counterparts. Considering the lattice parameters of TiB$_2$ and TaB$_2$ are smaller than others, the right part (SS1b) of SS1 should be assigned to the (Ti, Ta)-rich regions. The (Zr, Nb, Hf)-rich regions which contain more Hf should have the largest lattice parameters, which are supposed to be SS2. This is also in favor of the fact that SS2 is rich in Zr and Hf according to XRD patterns. On the contrary, the lattice parameters of (Zr, Nb)-rich regions position between the above two, which correspond to the left part of SS1 (SS1a). With the temperature increasing, the distribution of Hf became homogenous and not concentrated on specific particles (as seen in Figs 6, 7). This indicated the Hf in (Zr, Nb, Hf)-rich solid solution gradually diffused into the matrix, which was in well accordance with the weakened signal of SS2 as observed in Fig. 2d.

The sinterability of self-synthesized (Ti$_{0.2}$Hf$_{0.2}$Zr$_{0.2}$Nb$_{0.2}$Ta$_{0.2}$)B$_2$ powders

In order to evaluate the sinterability of the as-synthesized powders, HEB3-17 powders were selected to densify HEBs, due to the relatively finer particle size and better composition homogeneity in this batch. Relative density of the HEBs sintered at 1900, 2000, and 2050°C is 85.8%, 94.4%, and 97.9%, respectively. The HEB powders obtained from BCTR route in this work exhibited better sinterability than those prepared from the existing routes (e.g., high energy ball milling [22] and self-propagating high-temperature synthesis [25]). Fig. 8 shows the polished surface of these HEBs sintered at different temperatures. Pores with a black contrast and size of ~1 μm are visible on the sample sintered at 1900°C, and are mainly located at grain boundaries. Both XRD patterns (Fig. 9) and oxygen maps (Fig. S3) indicate that all these ceramics have formed into a single phase, without notable residual oxides. However, the oxides have been recently observed in the HEBs sintered from the powders synthesized *via* borothermal reduction [26].

Although a single HEB phase has formed, apart from the pores, areas with two contrasts could be clearly distinguished from the BSE image: the darker one is rich in Nb and Zr (Fig. 10a) while the elemental distribution in the lighter area seems to be homogenous. Similar phase separation was previously noticed in the HEB powders (Fig. 7). Again, it supported the conclusion that SS1 peak was contributed by both (Ti, Ta) and (Nb, Zr)-rich solid solution.

When the sintering temperature further rose to 2000 and 2050°C, the porosity was evidently reduced and the distribution of Nb and Zr became homogenous, i.e., the final pore removal occurred simultaneously with the further diffusion of Nb and Zr atom from its rich to depleted regions in (Ti$_{0.2}$Zr$_{0.2}$Hf$_{0.2}$Nb$_{0.2}$Ta$_{0.2}$)B$_2$ (Fig. 10b, c). Surprisingly, a sudden grain growth occurred when the sintering temperature was elevated from 2000 to 2050°C. The average grain sizes of HEB3 ceramics are 0.71 ± 0.14 μm (1900°C), 6.67 ± 1.20 μm (2000°C) and 41.2 ± 8.1 μm (2050°C), respectively. Such rapid grain growth from 2000 to 2050°C is contradictory with the existing knowledge that high configurational entropy lowers the grain boundary energy, thus lowering the driving force for grain growth in high entropy materials [46,47]. It has not been observed in diboride ceramics. The mechanism for such a rapid grain growth of HEBs is still unclear. One possible reason is that entropy alone might not be sufficient to stabilize the (Ti$_{0.2}$Zr$_{0.2}$Hf$_{0.2}$Nb$_{0.2}$Ta$_{0.2}$)B$_2$ boride solid solution phase, and the en-
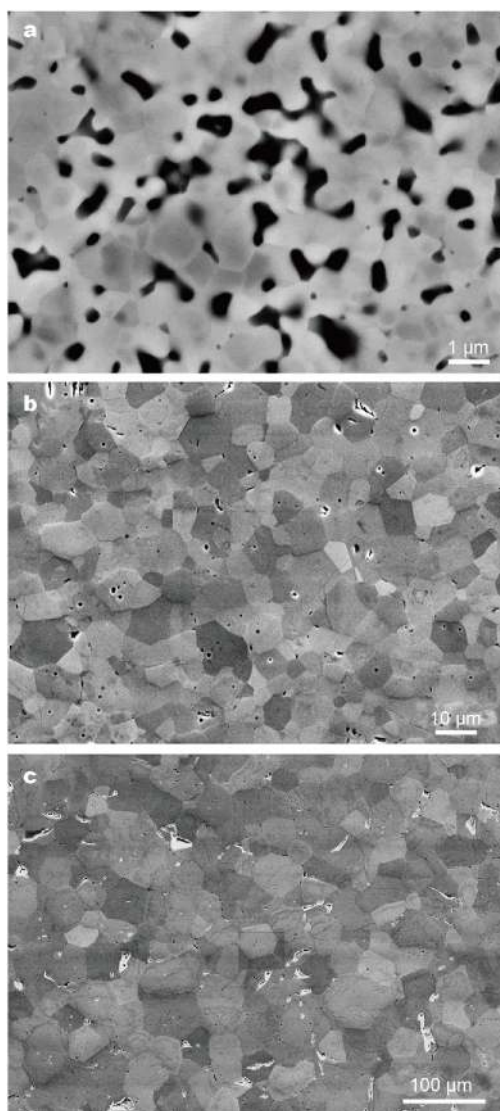
Figure 8 Polished surfaces of HEB3 ceramics sintered at (a) 1900°C, (b) 2000°C, and (c) 2050°C.

Figure 9 XRD patterns of the three ceramics.

thalpy of mixing in this system has to be evaluated to fully understand whether HEB is more stable compared with other single-phase counterparts.

The typical mechanical properties of the as-sintered HEB ceramics are summarized in Table 3. Young's modulus (E) of the HEB3 sintered at 2050°C (527 GPa) is slightly higher than that sintered at 2000°C (500 GPa), probably due to the less porosity in the former sample. The Vickers hardness of HEB3 ceramics sintered at 2000°C exhibits a typical indentation load dependence (ISE) behavior, i.e., the as-measured hardness values decrease with the increasing indentation load. ISE has been commonly observed in many structural ceramics [48].
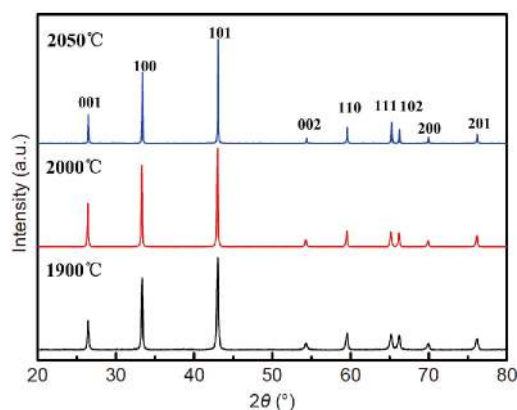
For example, under loads of 0.2, 1, and 5 kg, the hardness values for HEB3 are 25.61 ± 0.83, 22.44 ± 0.56 and 19.44 ± 0.50 GPa, respectively. These values are obviously higher than the results of previous reports on HEB ceramics with the same composition, e.g., 21.7 GPa under 0.2 kg [49] and 17.5 GPa under ~1 kg [22]. Such differences may be attributed to the high-purity and dense bulks achieved in this work. Apparently, any residual oxide and pores observed in references [22,49] will lower the hardness for HEB ceramics.

The hardness of each single phase diborides under the same indentation load is also compared in Table 3 [50–54]. The hardness of HEB ceramics (22.44 GPa under 1 kg load) is comparable to the averaged value (23.4 GPa, under 1 kg load) of the five. Considering the residual porosity left, higher intrinsic hardness value could be expected in HEB. Unfortunately, the fracture toughness of HEB shows no superiority or even worse than the other single-phase counterparts, possibly due to the lack of toughening mechanisms in this sample, as indicted by the cracks which propagated straightly in Fig. S1.

CONCLUSION

This work demonstrates that conventional boro/carbothermal reduction could be applied for the synthesis of HEB powders. $(Ti_{0.2}Hf_{0.2}Zr_{0.2}Nb_{0.2}Ta_{0.2})B_2$ powders were successfully synthesized by B_4C reduction of corresponding oxide mixtures. As-synthesized powders showed fine particle size, high purity and good sinterability. The following conclusions can be drawn regarding this study on the powder preparation, densification and mechanical properties of HEB ceramics:

(1) To minimize the residual oxide in the HEB powders, 10 wt% excess B_4C according to Reaction (1) has to be added in the starting powder mixtures, as the forma-
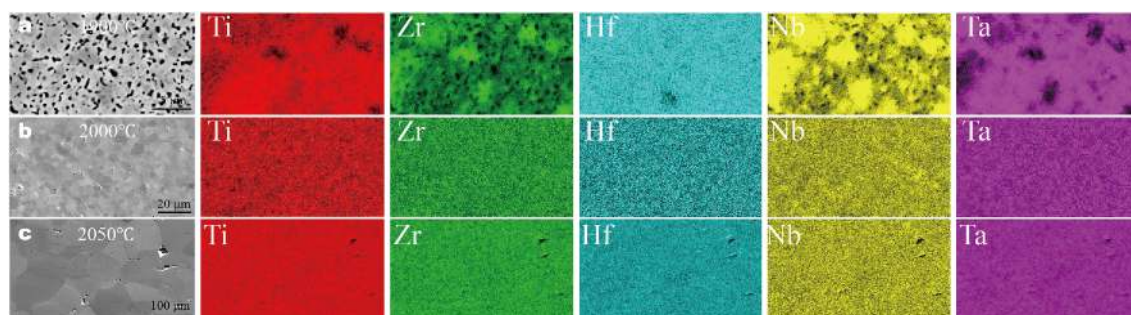
Figure 10 WDS-mappings of the specimens sintered at (a) 1900°C, (b) 2000°C, and (c) 2050°C, indicating the uneven elemental distribution at 1900°C while the elemental distributions at 2000 and 2050°C are homogenous.

Table 3 Properties of the high-entropy diboride ceramics

Composition	Sintering temperature (°C)	Relative density (%)	Average grain size (μm)	E (GPa)	K_{IC} (MPa m$^{1/2}$)	Hardness (GPa)	Ref.
$(Ti_{0.2}Zr_{0.2}Nb_{0.2}Hf_{0.2}Ta_{0.2})B_2$	2000	94.4	6.67 ± 1.20	500	2.83 ± 0.15	25.61 ± 0.83 (HV0.2) 22.44 ± 0.56 (HV1)	This work
$(Ti_{0.2}Zr_{0.2}Nb_{0.2}Hf_{0.2}Ta_{0.2})B_2$	2050	97.9	41.2 ± 8.1	527	/	26.82 ± 1.77 (HV0.2)	This work
$(Ti_{0.2}Zr_{0.2}Nb_{0.2}Hf_{0.2}Ta_{0.2})B_2$	2000	92.4	/	/	/	17.5 ± 1.2 (HV~1)	[22]
$(Ti_{0.2}Zr_{0.2}Nb_{0.2}Hf_{0.2}Ta_{0.2})B_2$	2000	96.3	1.59	/	4.06 ± 0.35	21.7 ± 1.1 (HV0.2)	[49]
TiB_2	1800	96.1	/	497 ± 15	4.64 ± 0.45	28.6-32.4 (HV1)	[50]
ZrB_2	2000	99.8	~6	489	3.5 ± 0.3	23 ± 0.9 (HV1)	[51]
NbB_2	1900	97.7	/	539	4.0 ± 0.6	20.3 ± 0.6 (HV0.5)[a]	[52]
HfB_2	1850	98.8	8	/	3.5 ± 0.5	18.1 ± 0.9 (HV1)	[53]
TaB_2	1850	96	5.3	/	5.61 ± 0.17	25.1 ± 0.5 (HV1)	[54]

a) HV1 data is not available.

tion of BO(g) (Reaction 2) will consume more B_4C.

(2) All the oxides could be reduced by B_4C in mild vacuum at as low as 1500°C in this system. Study of the solid solution process showed that different solid solution, i.e., (i) TiB_2 dominated; (ii) (Ti, Ta)-rich; (iii) (Zr, Hf, Nb)-rich and (iv) (Zr, Nb)-rich, appeared during the BCTR process. Homogenization of them cannot be realized until the as-synthesized HEB powders were sintered at 2000°C or above.

(3) Powders synthesized at 1700°C (HEB3-17) exhibit relatively good sinterability. Single phase HEBs with high relative density of 94.4% were achieved at 2000°C/50 MPa /5 min using this powder. Corresponding $(Ti_{0.2}Hf_{0.2}Zr_{0.2}Nb_{0.2}Ta_{0.2})B_2$ ceramics exhibits a combination of good mechanical properties, except fracture toughness, including a hardness of 22.44 ± 0.56 GPa, a fracture toughness of 2.83 ± 0.15 MPa m$^{1/2}$ and a Young's modulus of 500 GPa.

(4) Rapid grain growth for HEBs was found on the samples sintered at 2050°C, suggesting the high configurational entropy might not be enough to stabilize the

$(Ti_{0.2}Zr_{0.2}Hf_{0.2}Nb_{0.2}Ta_{0.2})B_2$ ceramics at ultra-high temperature.

1 Yeh JW, Chen SK, Lin SJ, *et al*. Nanostructured high-entropy alloys with multiple principal elements: novel alloy design concepts and outcomes. Adv Eng Mater, 2004, 6: 299–303

2 Zhang Y, Zuo TT, Tang Z, *et al*. Microstructures and properties of high-entropy alloys. Prog Mater Sci, 2014, 61: 1–93

3 Zhang W, Liaw PK, Zhang Y. Science and technology in high-entropy alloys. Sci China Mater, 2018, 61: 2–22

4 Rost CM, Sachet E, Borman T, *et al*. Entropy-stabilized oxides. Nat Commun, 2015, 6: 8485

5 Bérardan D, Franger S, Meena AK, *et al*. Room temperature lithium superionic conductivity in high entropy oxides. J Mater Chem A, 2016, 4: 9536–9541

6 Bérardan D, Franger S, Dragoe D, *et al*. Colossal dielectric constant in high entropy oxides. Phys Status Solidi RRL, 2016, 10: 328–333

7 Rost CM, Rak Z, Brenner DW, *et al*. Local structure of the $Mg_xNi_xCo_xCu_xZn_xO$ ($x = 0.2$) entropy-stabilized oxide: An EXAFS study. J Am Ceram Soc, 2017, 100: 2732–2738

8 Meisenheimer PB, Kratofil TJ, Heron JT. Giant enhancement of exchange coupling in entropy-stabilized oxide heterostructures. Sci

Rep, 2017, 7: 13344

9 Jiang S, Hu T, Gild J, *et al.* A new class of high-entropy perovskite oxides. Scripta Mater, 2018, 142: 116–120

10 Sarkar A, Velasco L, Wang D, *et al.* High entropy oxides for reversible energy storage. Nat Commun, 2018, 9: 3400

11 Braun JL, Rost CM, Lim M, *et al.* Charge-induced disorder controls the thermal conductivity of entropy-stabilized oxides. Adv Mater, 2018, 30: 1805004

12 Sarkar A, Djenadic R, Wang D, *et al.* Rare earth and transition metal based entropy stabilised perovskite type oxides. J Eur Ceramic Soc, 2018, 38: 2318–2327

13 Anand G, Wynn AP, Handley CM, *et al.* Phase stability and distortion in high-entropy oxides. Acta Mater, 2018, 146: 119–125

14 Hong W, Chen F, Shen Q, *et al.* Microstructural evolution and mechanical properties of (Mg,Co,Ni,Cu,Zn)O high-entropy ceramics. J Am Ceram Soc, 2018, 375: jace.16075

15 Castle E, Csanádi T, Grasso S, *et al.* Processing and properties of high-entropy ultra-high temperature carbides. Sci Rep, 2018, 8: 8609

16 Sarker P, Harrington T, Toher C, *et al.* High-entropy high-hardness metal carbides discovered by entropy descriptors. Nat Commun, 2018, 9: 4980

17 Yan X, Constantin L, Lu Y, *et al.* $(Hf_{0.2}Zr_{0.2}Ta_{0.2}Nb_{0.2}Ti_{0.2})C$ high-entropy ceramics with low thermal conductivity. J Am Ceram Soc, 2018, 101: 4486–4491

18 Dusza J, Švec P, Girman V, *et al.* Microstructure of (Hf-Ta-Zr-Nb)C high-entropy carbide at micro and nano/atomic level. J Eur Ceramic Soc, 2018, 38: 4303–4307

19 Feng L, Fahrenholtz WG, Hilmas GE, *et al.* Synthesis of single-phase high-entropy carbide powders. Scripta Mater, 2019, 162: 90–93

20 Harrington TJ, Gild J, Sarker P, *et al.* Phase stability and mechanical properties of novel high entropy transition metal carbides. Acta Mater, 2019, 166: 271–280

21 Ye B, Wen T, Huang K, *et al.* First-principles study, fabrication, and characterization of $(Hf_{0.2}Zr_{0.2}Ta_{0.2}Nb_{0.2}Ti_{0.2})C$ high-entropy ceramic. J Am Ceram Soc, 2019, 102: 4344–4352

22 Gild J, Zhang Y, Harrington T, *et al.* High-entropy metal diborides: A new class of high-entropy materials and a new type of ultrahigh temperature ceramics. Sci Rep, 2016, 6: 37946

23 Wang YP, Gan GY, Wang W, *et al. Ab initio* prediction of mechanical and electronic properties of ultrahigh temperature high-entropy ceramics $(Hf_{0.2}Zr_{0.2}Ta_{0.2}M_{0.2}Ti_{0.2})B_2$ (M = Nb, Mo, Cr). Phys Status Solidi B, 2018, 255: 1800011

24 Mayrhofer PH, Kirnbauer A, Ertelthaler P, *et al.* High-entropy ceramic thin films: A case study on transition metal diborides. Scripta Mater, 2018, 149: 93–97

25 Tallarita G, Licheri R, Garroni S, *et al.* Novel processing route for the fabrication of bulk high-entropy metal diborides. Scripta Mater, 2019, 158: 100–104

26 Zhang Y, Guo WM, Jiang ZB, *et al.* Dense high-entropy boride ceramics with ultra-high hardness. Scripta Mater, 2019, 164: 135–139

27 Lai CH, Lin SJ, Yeh JW, *et al.* Preparation and characterization of AlCrTaTiZr multi-element nitride coatings. Surf Coatings Tech, 2006, 201: 3275–3280

28 Hsieh MH, Tsai MH, Shen WJ, *et al.* Structure and properties of two Al–Cr–Nb–Si–Ti high-entropy nitride coatings. Surf Coatings Tech, 2013, 221: 118–123

29 Jin T, Sang X, Unocic RR, *et al.* Mechanochemical-assisted

synthesis of high-entropy metal nitride *via* a soft urea strategy. Adv Mater, 2018, 30: 1707512

30 Qin Y, Liu JX, Li F, *et al.* A high entropy silicide by reactive spark plasma sintering. J Adv Ceram, 2019, 8: 148–152

31 Dai FZ, Zhou Y, Sun W. Segregation of solute atoms (Y, Nb, Ta, Mo and W) in ZrB_2 grain boundaries and their effects on grain boundary strengths: A first-principles investigation. Acta Mater, 2017, 127: 312–318

32 Ran S, Van der Biest O, Vleugels J. ZrB_2 powders synthesis by borothermal reduction. J Am Ceramic Soc, 2010

33 Guo WM, Zhang GJ. Reaction processes and characterization of ZrB_2 powder prepared by boro/carbothermal reduction of ZrO_2 in vacuum. J Am Ceramic Soc, 2009, 92: 264–267

34 Zhao H, He Y, Jin Z. Preparation of zirconium boride powder. J Am Ceramic Soc, 1995, 78: 2534–2536

35 Zeng L, Wei W, Sun S, *et al.* Powder characteristics, sinterability, and mechanical properties of TiB_2 prepared by three reduction methods. J Am Ceramic Soc, 2019, 102: 4511–4519

36 You Y, Tan DW, Guo WM, *et al.* TaB_2 powders synthesis by reduction of Ta_2O_5 with B_4C. Ceramics Int, 2017, 43: 897–900

37 Feng L, Kim JM, Lee SH, *et al.* Synthesis of a fine $(Ta_{0.8}Hf_{0.2})C$ powder from carbide or oxide powder mixtures. J Am Ceram Soc, 2016, 99: 1129–1132

38 Wang H, Lee SH, Kim HD, *et al.* Nano-hafnium diboride powders synthesized using a spark plasma sintering apparatus. J Am Ceram Soc, 2012, 95: 1493–1496

39 Xie J, Fu Z, Wang Y, *et al.* Synthesis of nanosized zirconium carbide powders by a combinational method of sol–gel and pulse current heating. J Eur Ceramic Soc, 2014, 34: 13.e1–13.e7

40 Wang R, Wang Y, Fu Z, *et al.* Spark plasma sintering of transparent YAG ceramics assisted by the YAH–YAG phase transformation. J Eur Ceramic Soc, 2016, 36: 2153–2156

41 Rietveld HM. Line profiles of neutron powder-diffraction peaks for structure refinement. Acta Cryst, 1967, 22: 151–152

42 Toby BH. *EXPGUI*, a graphical user interface for *GSAS*. J Appl Crystlogr, 2001, 34: 210–213

43 Evans AG, Charles EA. Fracture toughness determinations by indentation. J Am Ceram Soc, 1976, 59: 371–372

44 Avilés MA, Córdoba JM, Sayagués MJ, *et al.* Mechanosynthesis of $Hf_{1-x}Zr_xB_2$ solid solution and $Hf_{1-x}Zr_xB_2$/SiC composite powders. J Am Ceramic Soc, 2010, 93: 696–702

45 Liu D, Wen T, Ye B, *et al.* Molten salt synthesis, characterization, and formation mechanism of superfine $(Hf_xZr_{1-x})B_2$ solid-solution powders. J Am Ceram Soc, 2019, 102: 3763–3770

46 Zhou N, Hu T, Huang J, *et al.* Stabilization of nanocrystalline alloys at high temperatures *via* utilizing high-entropy grain boundary complexions. Scripta Mater, 2016, 124: 160–163

47 Lei Z, Liu X, Wang H, *et al.* Development of advanced materials via entropy engineering. Scripta Mater, 2019, 165: 164–169

48 Zou J, Zhang GJ, Kan YM, *et al.* Hot-pressed ZrB_2-SiC ceramics with VC addition: chemical reactions, microstructures, and mechanical properties. J Am Ceram Soc, 2009, 92: 2838–2846

49 Zhang Y, Jiang ZB, Sun SK, *et al.* Microstructure and mechanical properties of high-entropy borides derived from boro/carbothermal reduction. J Eur Ceramic Soc, 2019, 39: 3920–3924

50 Mukhopadhyay A, Raju GB, Basu B, *et al.* Correlation between phase evolution, mechanical properties and instrumented indentation response of TiB_2-based ceramics. J Eur Ceramic Soc, 2009, 29: 505–516

51 Chamberlain AL, Fahrenholtz WG, Hilmas GE, *et al.* High-

strength zirconium diboride-based ceramics. J Am Ceramic Soc, 2004, 87: 1170–1172

52 Sairam K, Sonber JK, Murthy TSRC, *et al.* Reaction spark plasma sintering of niobium diboride. Int J Refractory Met Hard Mater, 2014, 43: 259–262

53 Ni DW, Zhang GJ, Kan YM, *et al.* Hot pressed HfB$_2$ and HfB$_2$-20 vol%SiC ceramics based on HfB$_2$ powder synthesized by bor-othermal reduction of HfO$_2$. Int J Appl Ceramic Tech, 2010, 7: 830–836

54 Licheri R, Orrù R, Musa C, *et al.* Synthesis, densification and characterization of TaB$_2$–SiC composites. Ceramics Int, 2010, 36: 937–941

Author contributions Zou J and Fu ZY designed the research. Gu J and Zou J performed the experiments with the help of Wang H, Wang W, Zhang J and Fu ZY. Sun SK performed the XRD refinement. Yu SY and Zou J performed the hardness test. Fu Z supervised and acquired funding for the research. Gu J and Zou J wrote the paper. All authors discussed the results and commented on the manuscript.

Conflict of interest These authors declare no conflict of interest.

Supplementary information Supporting data are available in the online version of this paper.

Junfeng Gu is currently a PhD student at the State Key Laboratory of Advanced Technology for Materials Synthesis and Processing, Wuhan University of Technology. His research focuses on the sintering mechanisms and properties of ultra-high temperature ceramics.

Ji Zou is a Research Fellow at the University of Birmingham, UK and an adjunct professor at Wuhan Institute of Technology, China. He received his PhD degree from Shanghai Institute of Ceramics, Chinese Academy of Sciences. He has been active in the processing-structure-property correlation of ceramics, especially for boride ceramics.

Zhengyi Fu is a chief professor at the State Key Laboratory of Advanced Technology for Materials Synthesis and Processing, Wuhan University of Technology. He received his PhD degree from Wuhan University of Technology in 1994. His current research interests include advanced sintering and bioprocess-inspired fabrication.

硼热/碳热还原技术制备高致密度、高纯度高熵硼化物陶瓷

顾俊峰[1]，邹冀[1,2*]，孙世宽[3]，王皓[1]，于苏洋[2]，张金咏[1]，王为民[1]，傅正义[1*]

摘要 以过渡金属氧化物(MO$_x$)和碳化硼(B$_4$C)为原料，采用硼热/碳热还原技术在1800°C下制备得到了等摩尔比的亚微米级五元高熵硼化物(Ti$_{0.2}$Hf$_{0.2}$Zr$_{0.2}$Nb$_{0.2}$Ta$_{0.2}$)B$_2$粉体，并深入探讨了硼热/碳热还原过程中产物的物相、形貌以及固溶体变化过程. X射线衍射谱表明所制备的粉体在1800°C即形成了单相结构，但直到2000°C样品中各元素才分布均匀. 将得到的粉体在2050°C/50 MPa的条件下进行放电等离子烧结，获得了相对密度为97.9%的高熵硼化物陶瓷. 研究发现，当烧结温度从2000°C增加到2050°C时，高熵陶瓷晶粒迅速长大，平均晶粒尺寸从6.67 μm增大到41.2 μm. 2000°C下制备得到的高熵硼化物陶瓷具有良好的力学性能，其硬度、杨氏模量和断裂韧性分别为22.44 ± 0.56 GPa，~500 GPa，2.83 ± 0.15 MPa m$^{1/2}$.